Comparison of space-time evolutions of hot, dense matter in $\sqrt{s_{NN}}=17$ and 130 GeV relativistic heavy ion collisions based on a hydrodynamical model

Kenji Morita,[1,*] Shin Muroya,[2,†] Chiho Nonaka,[3,‡] and Tetsufumi Hirano[4,§]

[1]*Department of Physics, Waseda University, Tokyo 169-8555, Japan*
[2]*Tokuyama Women's College, Tokuyama, Yamaguchi 745-8511, Japan*
[3]*The Institute of Physical and Chemical Research (RIKEN), Wako, Saitama, 351-0198, Japan*
[4]*Physics Department, University of Tokyo, Tokyo 113-0033, Japan*

Based on a hydrodynamical model, we compare 130 GeV/nucleon Au+Au collisions at the Relativistic Heavy Ion Collider (RHIC) and 17 GeV/nucleon Pb+Pb collisions at the Super Proton Synchrotron (SPS). The model well reproduces the single-particle distributions of both the RHIC and SPS. The numerical solution indicates that a huge amount of collision energy in the RHIC is mainly used to produce a large extent of hot fluid rather than to make a high temperature matter; the longitudinal extent of the hot fluid in the RHIC is much larger than that of the SPS and the initial energy density of the fluid is only 5% higher than the one in the SPS. The solution well describes the HBT radii at the SPS energy but shows some deviations from the ones at the RHIC.

I. INTRODUCTION

One of the main purposes of ultrarelativistic heavy ion collision experiments is to explore the property of the hot and dense matter [1]. Recently the new experiment has begun to work at the Brookhaven National Laboratory Relativistic Heavy-Ion Collider (RHIC) of which higher collision energy than other experiments up to now provides us chances to produce a new state of matter, quark-gluon plasma (QGP), with distinct possibility. However, the complicated collision processes composed of multiparticle productions and many-body interactions make it difficult to understand the properties of the hot matter. Therefore, a simple dynamical description of the system as a basis for deeper understanding is indispensable.

Relativistic hydrodynamical models are well-established phenomenological tools for describing high energy nucleus-nucleus collisions and subsequent multiparticle production [2–8]. In this paper, we use a $(3+1)$-dimensional hydrodynamical model [9] with a QCD phase transition. We assume a cylindrical symmetry to the collision dynamics. Thus, our discussion is limited to the central collisions only. By virtue of the simple picture of our model, we can easily analyze both Super Proton Synchrotron (SPS) and RHIC data with the same numerical code. Most of hydrodynamical calculations for RHIC data use Bjorken's scaling solution [2] for the longitudinal direction. For example, Kolb *et al.* analyzed hadronic tranverse mass spectra and anisotropic flow [10]. Zschiesche *et al.* [11] investigated the HBT radii. These calculations assume the longitudinal boost-invariant infinite source. Though recently some hybrid models are used [12–14] for the description of the hadronic phase, here we use a conventional description in which the hadronic phase is in local equilibrium.

In this paper, concentrating our discussion on the central collisions, we reproduce the single-particle spectra of hadrons at the beginning. In the hydrodynamical model, single-particle distributions are used as inputs rather than outputs in order to determine initial parameters. However, it is not trivial whether we succeed in reproducing experiments with "natural parameters" or not. Based on the solutions of hydrodynamical equations, we discuss the physical properties and the space-time evolution of the fluids in the SPS and RHIC. We also evaluate the two-pion correlation functions and analyze the HBT radii. As a subsequent work of Ref. [15], we focus our discussion on comparison of the RHIC results and the SPS results based on the same numerical code.

As is well known, the two-particle correlation function gives us information on the size of the particle source [16,17]. In the cases of the relativisitic heavy ion collisions, the correlation function tells us about the freeze-out which should be far from the static source. Thus, dynamical models such as hydrodynamical models are indispensable for understanding the relation between observed correlation functions and the space-time history of the system. However, up to now, any dynamical model assuming QGP failed to explain the experimental HBT radii in the RHIC consistently with the single-particle spectra [11,18] and elliptic flow [19], known as the "HBT puzzle."[1] We study the HBT radii in the framework of a hydrodynamical model which takes account of both transverse and longitudinal flow appropriately with a simple initial condition.

In the next section, we explain our model. In Sec. III, we discuss the space-time evolution of the fluid. In Sec. IV, we present the result of the two-particle correlation. Section V is devoted to concluding remarks.

II. HYDRODYNAMICAL MODEL

Let the system achieve the local thermal and chemical equilibrium shortly after a collision of two incident nuclei.

*Electronic address: morita@hep.phys.waseda.ac.jp
†Electronic address: muroya@yukawa.kyoto-u.ac.jp
‡Electronic address: nonaka@rarfaxp.riken.go.jp
§Electronic address: hirano@nt.phys.s-u-tokyo.ac.jp

[1]In Ref. [20], a hadronic rescattering model is shown to reproduce these quantities.

This relaxation process cannot be described by the hydrodynamical model. The hydrodynamical model starts at an initial time, τ_0, at which thermal and chemical equilibrium are established at least locally. The hydrodynamical equations are given as

$$\partial_\mu T^{\mu\nu} = 0. \tag{1}$$

We assume the perfect fluid for simplicity. Hence, the energy-momentum tensor is given as

$$T^{\mu\nu} = (\varepsilon + P)U^\mu U^\nu - Pg^{\mu\nu}, \tag{2}$$

with U^μ, ε, and P being four velocities of a fluid element, energy density, and pressure, respectively. These are treated as local quantities. We numerically solve the above equations together with the net baryon number conservation law,

$$\partial_\mu(n_B U^\mu) = 0, \tag{3}$$

where n_B is the net baryon number density and is also treated as a local quantity. Putting the z axis as a collision axis, we use a cylindrical coordinate system as follows:

$$t = \tau \cosh \eta, \tag{4}$$

$$x = r \cos \phi, \tag{5}$$

$$y = r \sin \phi, \tag{6}$$

$$z = \tau \sinh \eta. \tag{7}$$

Focusing our discussion on central collisions, we may assume the cylindrical symmetry on the system. Therefore, by virtue of an identity $U_\mu U^\mu = 1$, the four velocity can be expressed by two rapiditylike variables Y_L and Y_T:

$$U^\tau = \cosh(Y_L - \eta)\cosh Y_T, \tag{8}$$

$$U^\eta = \sinh(Y_L - \eta)\cosh Y_T, \tag{9}$$

$$U^r = \sinh Y_T. \tag{10}$$

Most of hydrodynamical calculations which analyze RHIC data use Bjorken's scaling solution $Y_L = \eta$. Putting the solution as an ansatz reduces numerical tasks very much but the analyses are limited to the midrapidity region only. We solve not only transverse expansion but also the longitudinal expansion explicitly. The numerical procedure for solving coupled Eqs. (1) and (3) is explained in Ref. [9]. In this algorythm, we solve the entropy and baryon number conservation law explicitly. Throughout our calculation, the total energy, entropy, and baryon number are conserved within 5% of accuracy at the time step $\delta\tau = 0.01$ fm/c.

In order to solve the hydrodynamical equations, we must fix the equation of state (EOS). We adopt a bag model EOS with a first order phase transition. The QGP phase is composed of a free gas of massless u, d, and s quarks and gluons. The hadronic phase is also assumed to be a free gas but with excluded volume correction. All hadrons are included up to 2 GeV/c^2 of mass except for hyperons. Putting the critical
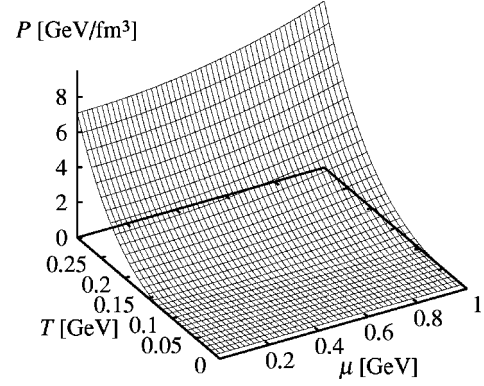

FIG. 1. Pressure $P(T,\mu_B)$ distribution.

temperature as $T_c = 160$ MeV at vanishing baryon density, we get the bag constant $B^{1/4} = 233$ MeV. We display the pressure as a function of temperature and baryonic chemical potential in Fig. 1. See Ref. [21] for further details of the EoS and numerical treatment of the first order phase transition in solving the hydrodynamical equations.

We assume that the system achieves local equilibrium and begins to expand hydrodynamically at $\tau = \tau_0 = 1.0$ fm/c. We put the initial conditions on this hyperbola. Bjorken's scaling solution is used as the initial condition of the longitudinal flow. Transverse flow is simply neglected at the initial time. We parametrize the initial energy density distribution $\varepsilon(\tau_0,\eta,r)$ and net baryon number density distribution $n_B(\tau_0,\eta,r)$ as

$$\varepsilon(\tau_0,\eta,r) = \varepsilon_{\max}\exp\left[-\frac{(|\eta|-\eta_0)^2}{2\cdot\sigma_\eta^2}\theta(|\eta|-\eta_0) \right.$$
$$\left. -\frac{(r-r_0)^2}{2\cdot\sigma_r^2}\theta(r-r_0) \right], \tag{11}$$

$$n_B(\tau_0,\eta,r) = n_{B0}\left\{ \exp\left[-\frac{(\eta-\eta_D)^2}{2\cdot\sigma_D^2} \right] + \exp\left[-\frac{(\eta+\eta_D)^2}{2\cdot\sigma_D^2} \right] \right\}$$
$$\times \exp\left[-\frac{(r-r_0)^2}{2\cdot\sigma_r^2}\theta(r-r_0) \right]. \tag{12}$$

The energy density distribution of the longitudinal direction (11) has a central plateau characterized by η_0 and a Gaussian tail whose width is given by σ_η (Fig. 2), while the net baryon number distribution is a superposition of the two Gaussians in which peaks exist at $\pm\eta_D$. For the transverse direction, both are parametrized by a flat region with Gaussian smearing near the edge (Fig. 3). For a nucleus with mass number A, the relation among these quantities is given by $\sigma_r + r_0 = 1.2A^{1/3}$.[2] Once these parameters are fixed, we can solve the hydrodynamical equations and pursue the space-

---

[2] We adopt the initial condition as a natural and the simplest extension of the $(1+1)$-dimensional Bjorken's picture (Ref. [2]) and as a basis for further improvement.
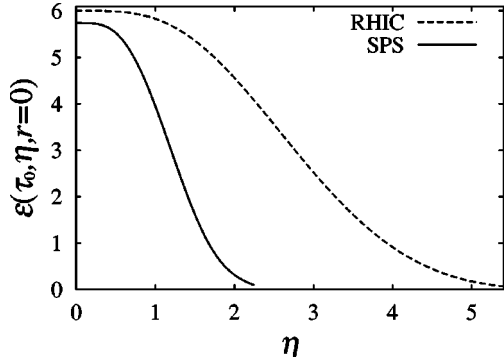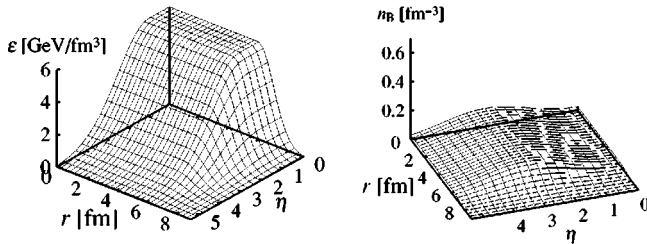
FIG. 2. Initial energy density distribution at $r=0$ in η direction. Dashed line stands for the RHIC case while solid line stands for the SPS case.

time evolution of the fluid. These initial parameters are so chosen that the model reproduces the single-particle spectra measured in the experiments. The single-particle spectra can be calculated by making use of of the Cooper-Frye formula [22]

$$E_{\mathbf{k}}\frac{dN_i}{d^3\mathbf{k}} = \frac{g_i}{(2\pi)^3}\int_\Sigma k_\mu d\sigma^\mu \frac{1}{\exp[(U_\nu k^\nu - \mu_B)/T_f]\mp 1},$$
(13)

where g_i is a degeneracy of the hadrons and T_f is a freeze-out temperature. The sign is plus for fermions and minus for bosons. Integration is performed on three-dimensional freeze-out hypersurface Σ. By virtue of the Lagrangian hydrodynamics, contribution from the timelike hypersurface is expected to be small and the spacelike hypersurface dominates the particle emission at freeze-out; we employ the non-covariant prescription $k_\mu d\sigma^\mu \simeq k_\tau d\sigma^\tau$ for the sake of simplicity in the numerical treatment. In this approximation, the

for RHIC 130A GeV Au+Au

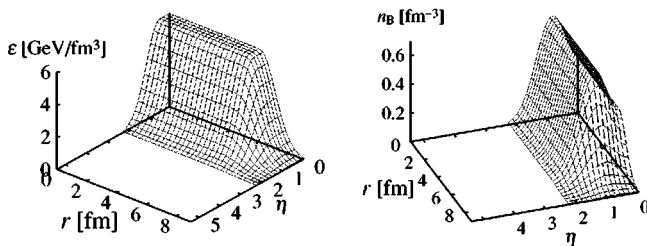### for SPS 17A GeV Pb+Pb

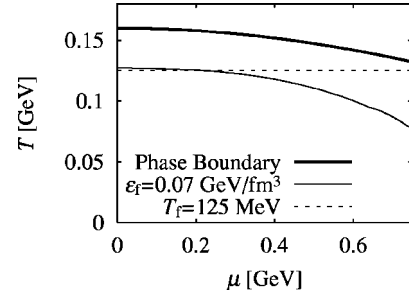FIG. 3. Initial energy density (left) and net baryon number density (right) distribution for the RHIC and SPS.

FIG. 4. Phase boundary (thick line) and freeze-out lines on T-μ_B plane. Thin solid line denotes the constant energy density contour as a freeze-out condition in the SPS. Dashed line stands for constant temperature line, which is a freeze-out condition in relativistic heavy-ion collisions.

total counted energy evaluated from Eq. (13) is slightly larger than 90% of the total energy of the initial fluid; the approximation works well enough. At the SPS, we assume that the freeze-out occurs at a energy density ε_f and at a temperature T_f, at the RHIC energy. We also assume that the thermal and the chemical freeze-out are taken to happen simultaneouly. We show the freeze-out lines and the phase boundary on the T-μ_B plane in Fig. 4. Note that two freeze-out lines in the figure do not differ at low baryonic chemical potential (Fig. 4).

We take account of the particles emitted from resonance decay as well as the direct emission from the freeze-out hypersurface. We include the decay processes $\rho \to 2\pi$, $\omega \to 3\pi$, $\eta \to 3\pi$, $K^* \to \pi K$, and $\Delta \to N\pi$ [23,24]. These resonances are also assumed to be thermally emitted from the freeze-out hypersurface.

Two sets of initial parameters are summarized in Table I. Figures 5–7 show single-particle spectra in 17A GeV Pb +Pb collisions at the SPS. Our model reproduces well the experimental data with parameters in Table I. Also in 130A GeV Au+Au collisions, our model shows good agreement with the data as in Figs. 8–11. However, we note that our model fails to produce enough antiprotons and overestimates the kaon yield in Fig. 10, where we multiply factors of 0.6 for kaons and 3.5 for antiprotons for clear comparison of the slopes [15]. This discrepancy may indicate the need for a more sophisticated freeze-out mechanism.

III. SPACE-TIME EVOLUTION

In this section, we present the numerical solution of the hydrodynamical equations and discuss differences in the space-time evolutions of the fluids between the RHIC and SPS. Figures 12 and 13 show space-time evolution of the fluid on the transverse plane. We also display the space-time evolution on the longitudinal plane in Fig. 14. Longitudinal flow and transverse flow are shown in Figs. 15 and 16, respectively. From Table I, the maximum energy density in the RHIC is only 5% higher than the one in the SPS. Only 5% higher energy density for the almost 50% larger dN/dY seems a surprising result. We show the number density of the thermal negative pions emitted into midrapidity as a function of the space-time rapidity η of the freeze-out point (Fig. 17).

TABLE I. Initial parameter set.

	SPS Pb+Pb	RHIC Au+Au
Maximum initial energy density ε_{max}	5.74 GeV/fm^3	6.0 GeV/fm^3
"Maximum" initial net baryon density n_{B0}	0.7 fm^{-3}	0.125 fm^{-3}
Longitudinal Gaussian width σ_η of initial energy density	0.61	1.47
Longitudinal extension η_0 of the flat region in the initial energy density	0.48	1.0
Longitudinal Gaussian width σ_D of the initial net baryon density	0.52	1.4
Space-time rapidity η_D at maximum of the initial net baryon distribution	0.82	3.0
Gaussian smearing parameter σ_r of the transverse profile	1.0 fm	1.0 fm
Freeze-out condition	$E_f = 70$ MeV/fm^3	$T_f = 125$ MeV

This figure informs us that the thermal contribution of the volume element at $\eta = 0$ to the particles into midrapidity is only 9% larger in the RHIC than in the SPS. However, the wider region of the freeze-out hypersurface in η contributes to the midrapidity particle distribution in the RHIC more than in the SPS. As a result, a 1.5 times larger number of particles obtained in the midrapidity region after summing up particles emitted at different η. The difference between the RHIC and SPS in Fig. 17 originates in the longitudinal extent $\eta_0 + \sigma_\eta$ (see also Fig. 2) and is direct consequence of longitudinal dynamics. We also plot the entropy per unit flow rapidity dS/dY_L in Fig. 18. This is a conserved quantity if the boost invariance is kept. In both the RHIC and SPS, reflecting the deviation from the scaling solution shown in Fig. 15, entropy is shifted to the larger flow rapidity. Reduction of entropy at $Y_L = 0$, where $Y_L = \eta = 0$ always holds, comes from $dY_L/d\eta$ which is larger than unity [25]. Thus, the shift at the RHIC is smaller than the one at the SPS since the deviation from the boost-invariant solution is small (Fig. 15). At the SPS, the difference of dS/dY_L between the initial stage and the final stage is larger than in the case at the RHIC.

Though our maximum energy density 6.0 GeV/fm^3 at the initial time is also much smaller than other calculation [10,11,26], this is due to the difference of the initial time and

transverse energy density profile of which nuclear thickness is considered. As for the average energy density at midrapidity, we get $\langle \varepsilon_{RHIC} \rangle = 3.9$ GeV/fm^3 and $\langle \varepsilon_{SPS} \rangle = 3.77$ GeV/fm^3. $\langle \varepsilon_{RHIC} \rangle$ is a little smaller than an estimation of Ref. [27]. As a result of such a small difference in energy density, the space-time evolutions of the two cases do not alter much in Figs. 12 and 13. The most different point is a longitudinal extension of the fluid, $\eta_0 + \sigma_\eta$. In the RHIC, it is twice as large as in the SPS. This is a consequence of much higher collision energy at the RHIC. Indeed, the total energy of the fluid is 25 290 GeV at the RHIC, which is 99% of the total collision energy. Hence, higher collision energy does not lead to higher energy density but is used to produce the matter with large volume at $\tau_0 = 1$ fm/c.

The output from the fluids is summarized in Table II. The total net baryon number of the fluid is much smaller in the RHIC than in the SPS, as well as the mean chemical potential on the freeze-out hypersurface. This difference can be seen in the space-time evolution of temperature on the η-τ plane (Fig. 14). As shown in Fig. 4, the phase boundary can no longer be specified by temperature only but depends on both temperature and chemical potential in high net baryon density. For example, $T = 158$ MeV corresponds to the hadronic phase at vanishing baryon density. However, it can be in the QGP phase at $\mu_B = 400$ MeV and in the mixed phase at some μ_B. This behavior is seen at the $T = 158$ MeV contour in Fig. 14, where the baryonic chemical potential be-
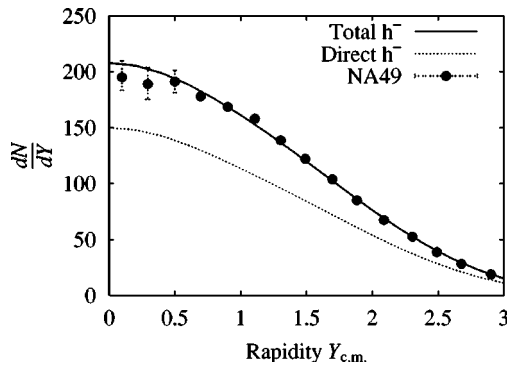

FIG. 5. Rapidity distribution of negatively charged hadrons in Pb+Pb collisions at the SPS. Closed circles are experimental data which are taken from Ref. [28]. Solid and dashed lines stand for our result of the total yield and contribution from direct particles.
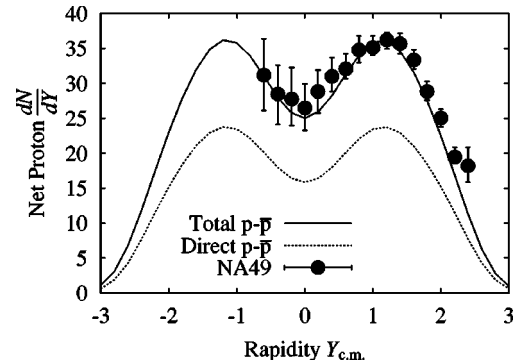

FIG. 6. Rapidity distribution of net protons in Pb+Pb collisions at the SPS. Meanings of symbols and lines are the same as in Fig. 5.
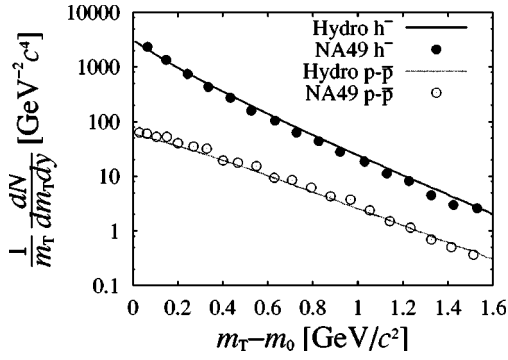
FIG. 7. Transverse mass distributions of negatively charged hadrons and net protons in Pb+Pb collisions at the SPS. Closed and open circles are the experimental data of negatively charged hadrons and net protons, respectively. Solid and dashed lines stand for charged hadrons and net protons of our result, respectively.
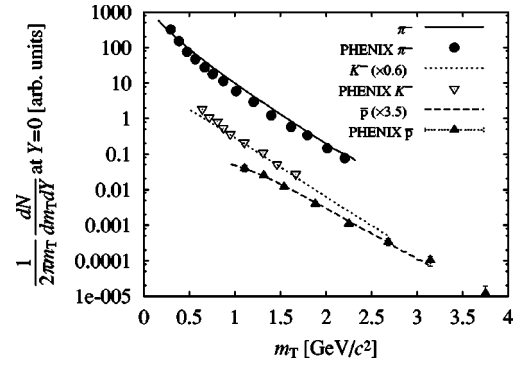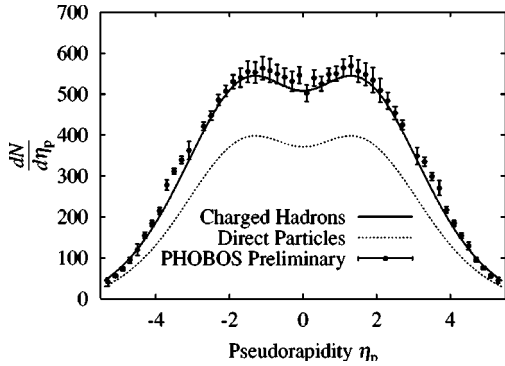
FIG. 8. Pseudorapidity η_p distribution of charged hadrons. Solid line shows our result (π, K, p) including resonance contribution. Dotted line denotes contribution of the directly emitted particles from the freeze-out hypersurface. Closed circles are preliminary result from the PHOBOS Collaboration (Ref. [29]).
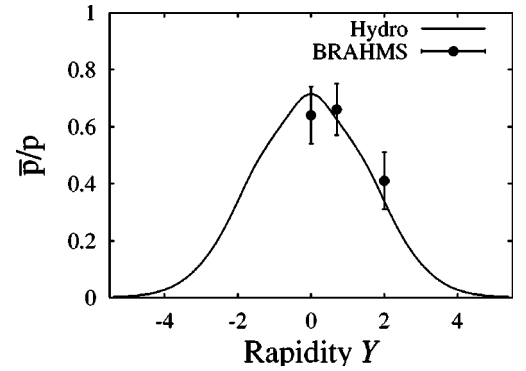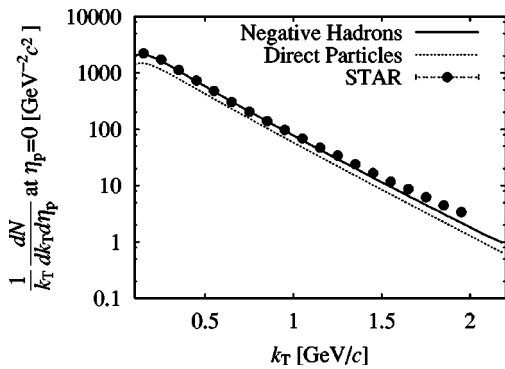
FIG. 9. Transverse momentum spectrum of negatively charged hadrons. As in Fig. 8, the solid line and dotted line show total number of particles and directly emitted particles from the freeze-out hypersurface, respectively. Closed circles are data from the STAR Collaboration (Ref. [30]).
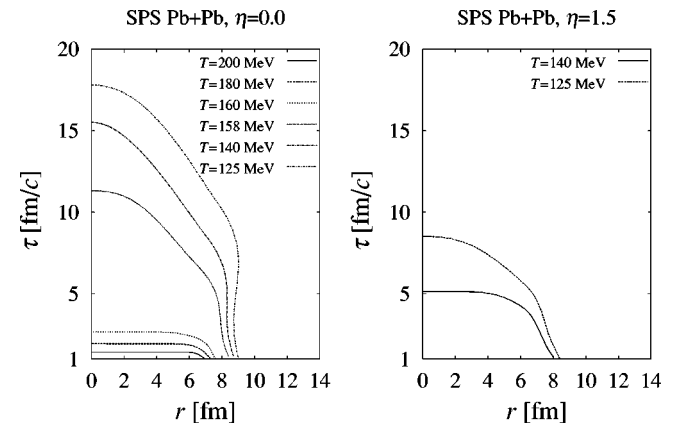
FIG. 10. Transverse mass spectra of negatively charged hadrons. Solid line, dotted line, and dashed line denote π^-, K^-, and $\bar{p}$ yields of our result. K^- and $\bar{p}$ spectra are scaled down by factors 0.1 and 0.01, respectively. Closed circles, open triangles, and closed triangles are preliminary data from the PHENIX Collaboration (Ref. [31]).

FIG. 11. Rapidity dependence of antiproton to proton ratio. Experimental data are taken from the BRAHMS Collaboration (Ref. [32]).

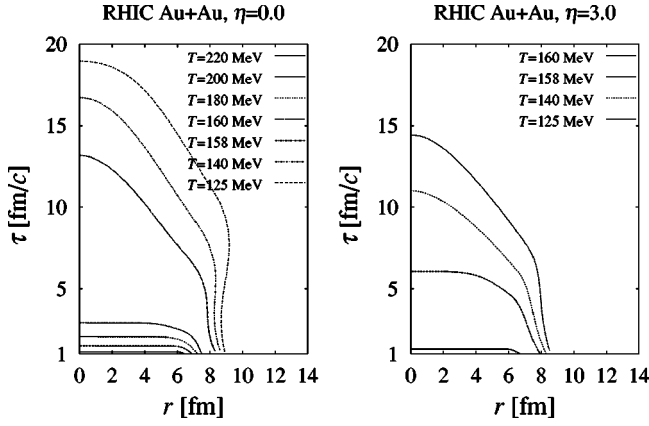FIG. 12. Temperature contour on r-τ plane at the SPS. Left: $\eta = 0$ section. Right: $\eta = 1.5$ section.

FIG. 13. Temperature contour on r-τ plane at the RHIC. Left: $\eta = 0$ section. Right: $\eta = 3.0$ section.
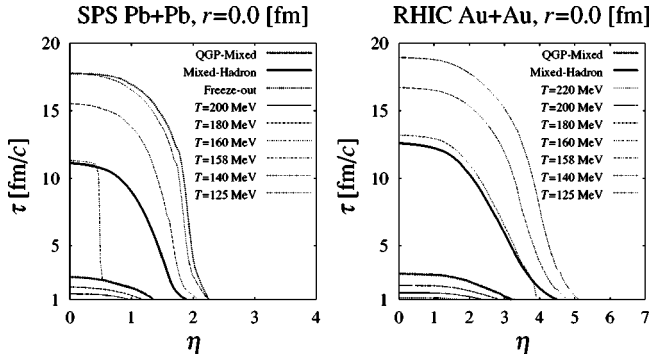

FIG. 14. Temperature contour on η-τ plane at $r = 0$ fm. Left figure shows the SPS case and right figure shows the RHIC case. Thick solid (dashed) line shows the phase boundary between mixed (QGP) phase and hadronic (mixed) phase. Freeze-out line is given as dotted line for the SPS. As for the RHIC, the $T_f = 125$ MeV contour corresponds to the freeze-out line.
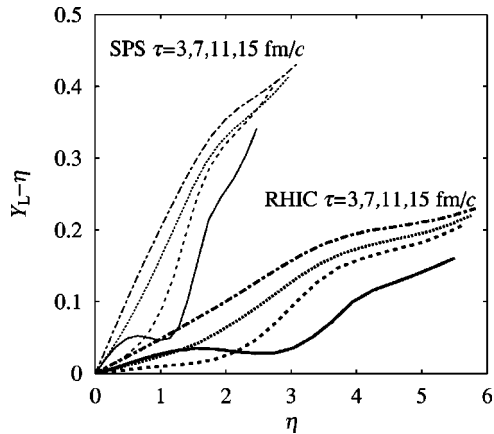

FIG. 15. Space-time evolution of longitudinal flow at $r = 0$. Deviation from Bjorken's scaling solution of longitudinal flow rapidity is plotted. Thick lines stand for the RHIC case and thin lines stand for the SPS case. In both cases, solid lines, dashed lines, dotted lines, and dash-dotted lines denote $\tau = 3, 7, 11$, and 15 fm/c cases, respectively.
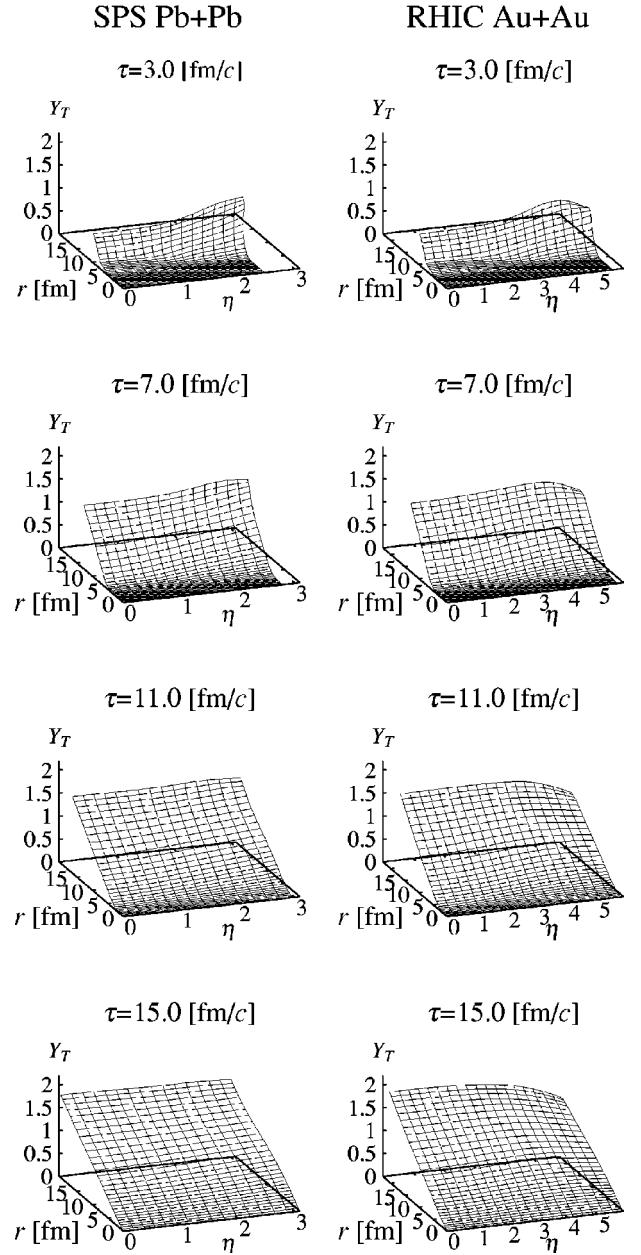

FIG. 16. Space-time evolution of transverse flow. Left and right columns show the SPS and the RHIC cases, respectively.

comes higher as η increases and a fluid element near $\eta \simeq 0.5$ stays at the mixed phase for a long time. Such behavior does not appear in the RHIC case where the chemical potential is small enough to characterize the mixed phase by the almost constant temperature.

In Fig. 15 where deviation from Bjorken's scaling solution $Y_L - \eta$ is plotted, acceleration is larger in the SPS than in the RHIC because of the steeper pressure gradient of the η direction. Finally, the lifetime of each phase is also shown in Table II.

IV. TWO-PARTICLE CORRELATION

In this section, we present the result of the two-pion correlation function and HBT radii based on the numerical so-
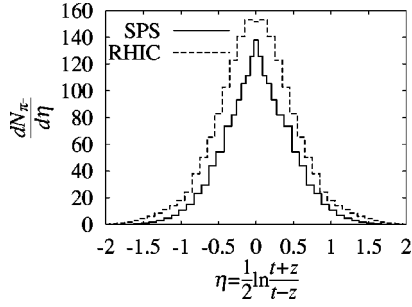
FIG. 17. Number density of the particles emitted into the midrapidity region as a function of space-time rapidity of the source point. Solid line stands for the SPS case and dashed line stands for the RHIC case.

lution of the relativistic hydrodynamical equation. For simplicity, we assume that all the pions are emitted from a chaotic source and neglect the resonance contribution. Then, the two-particle correlation function is easily calculated through

$$C_2(q^\mu, K^\mu) = 1 + \frac{|I(q^\mu, K^\mu)|^2}{I(0, k_1^\mu) I(0, k_2^\mu)}, \quad (14)$$

where $K^\mu = (k_1^\mu + k_2^\mu)/2$ and $q^\mu = k_1^\mu - k_2^\mu$ [33,34]. Here k_i^μ is the *on-shell* momentum of ith pion. We put

$$I(q^\mu, K^\mu) = \int K_\tau d\sigma^\tau(x) \sqrt{f(k_1, x) f(k_2, x)}\, e^{i q_\nu x^\nu}, \quad (15)$$

so that $I(0, k^\mu)$ reduces to the Cooper-Frye formula with $f(k, x)$ the Bose-Einstein distribution function. Considering the experimental momentum acceptance, we integrate the correlation function with respect to the average momentum in region Ω as

$$C_2(q^\mu)|_\Omega = 1 + \frac{\int_\Omega K_T dK_T dY |I(q^\mu, K^\mu)|^2}{\int_\Omega K_T dK_T dY\, I(0, k_1^\mu) I(0, k_2^\mu)}. \quad (16)$$

The HBT radii are obtained by fitting the calculated correlation function (16) to the Gaussian fitting function:

$$C_{2\mathrm{fit}}(q^\mu) = 1 + \exp(-R_{\mathrm{side}}^2 q_{\mathrm{side}}^2 - R_{\mathrm{out}}^2 q_{\mathrm{out}}^2 - R_{\mathrm{long}}^2 q_{\mathrm{long}}^2$$
$$- R_{\mathrm{ol}}^2 q_{\mathrm{out}} q_{\mathrm{long}}). \quad (17)$$

For RHIC data, in which rapidity acceptance $|Y| \leq 0.5$, the out-long cross term R_{ol} [35] can be ignored. According to the azimuthal symmetry, we can put $K_T = K_x$, $q_{\mathrm{side}} = q_y$, and $q_{\mathrm{out}} = q_x$.

Results of the HBT radii are presented in Figs. 19 and 20, where we show the transverse momentum dependence of the HBT radii of the SPS Pb+Pb collisions and $M_T \equiv \sqrt{K_T^2 + m_\pi^2}$ dependence of the RHIC Au+Au collisions,
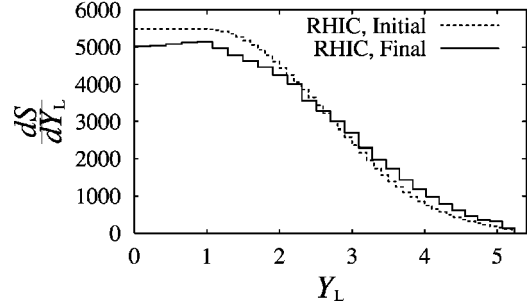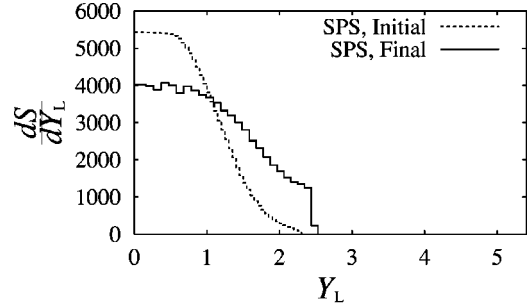

FIG. 18. Entropy per unit flow rapidity. In both figures (upper for the SPS and lower for the RHIC), solid lines stand for the quantities calculated on the freeze-out hypersurface and dashed lines stand for the one on the initial stage.

respectively. In addition to the three radius parameters, we also present the ratio of R_{out} to R_{side} for better comparison between two collisions [36].

Sideward HBT radii (upper figures in Figs. 19 and 20) are consistent with the experiments in both the RHIC and SPS. Larger radii than other calculations come from the initial large transverse size of the fluid. Outward HBT radii show quantitative agreement for the SPS data. However, qualitative behavior shows some deviation from the experimental data; our result takes the maximum value at $K_T \simeq 0.3$ GeV/c while the experiment data seem to monotonically decrease except for the highest K_T bin. For the RHIC data, experimental data show a steep decrease with M_T. On the other hand, our results are similar to the ones of the SPS because of the similarity in the space-time evolution of both fluids. As for the longitudinal HBT radii, our model reproduces the qualitative behavior of the results of both experiments but shows a little overestimate at low M_T of the RHIC result. Our result suggests that the longitudinal finite size effect is essential for understanding the behavior of R_{long} even at the RHIC because other calculations assuming an infinite boost-invariant source show larger R_{long} [11,19]. The HBT radius in the longitudinal direction has two kinds of origin: spatial extent of the fluid [35] and thermal suppression caused by rapid expansion. The emission region is roughly characterized by a product of the Boltzmann factor $\exp[-m_T \cosh(Y_L - Y)/T]$ and a geometrical factor [e.g., $\exp\{-\eta^2/2(\Delta \eta)^2\}$]. The deviation from the scaling solution causes stronger thermal suppression. As a result, our solution provides a smaller longitudinal HBT radius. Our $R_{\mathrm{out}}/R_{\mathrm{side}}$ moderately increases with K_T in both the SPS and RHIC. This tendency is also seen in a hybrid calculation [18] in spite of the quite different description of the hadronic phase.
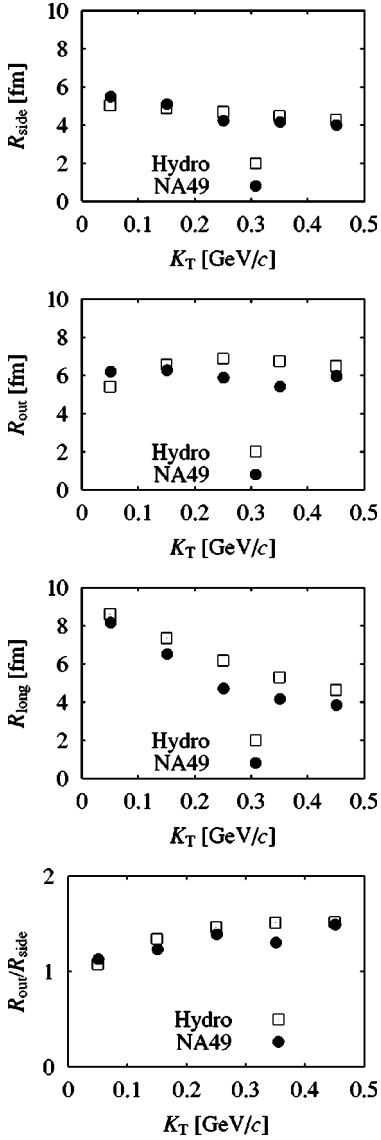
FIG. 19. HBT radii at the SPS. From top to bottom, R_{side}, R_{out}, R_{long}, and R_{out}/R_{side} are plotted. Closed circles denote the experimental data from the NA49 collaboration (Ref. [38]). Open squares stand for our results. Experimental acceptance is $2.9 \leq Y \leq 3.4$ in the laboratory system.
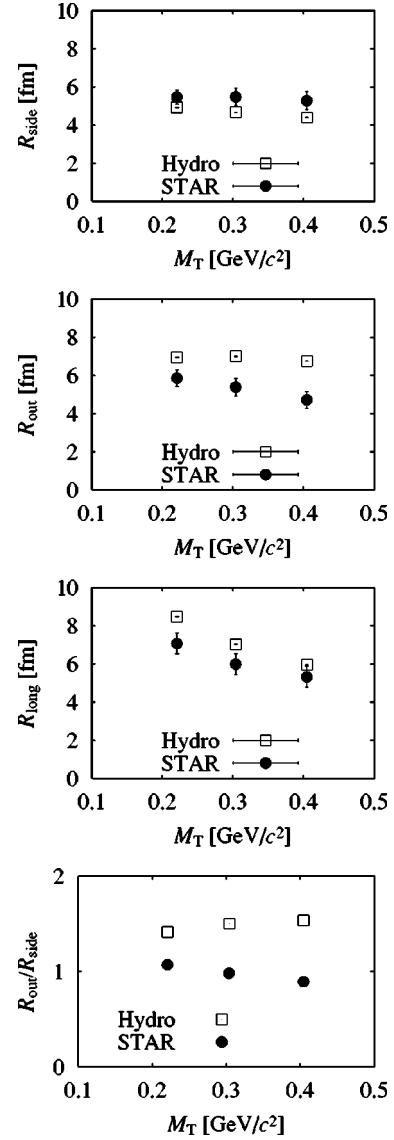
FIG. 20. HBT radii at the RHIC. From top to bottom, R_{side}, R_{out}, R_{long}, and R_{out}/R_{side} are plotted. Closed circles denote the experimental data from the STAR collaboration (Ref. [39]). Open squares stand for our results. Experimental rapidity acceptance is $|Y| \leq 0.5$. Three data points correspond to $0.125 \leq K_T \leq 0.225$ GeV/c, $0.225 \leq K_T \leq 0.325$ GeV/c, and $0.325 \leq K_T \leq 0.45$ GeV/c, respectively.

TABLE II. Output quantities from the numerical solutions.

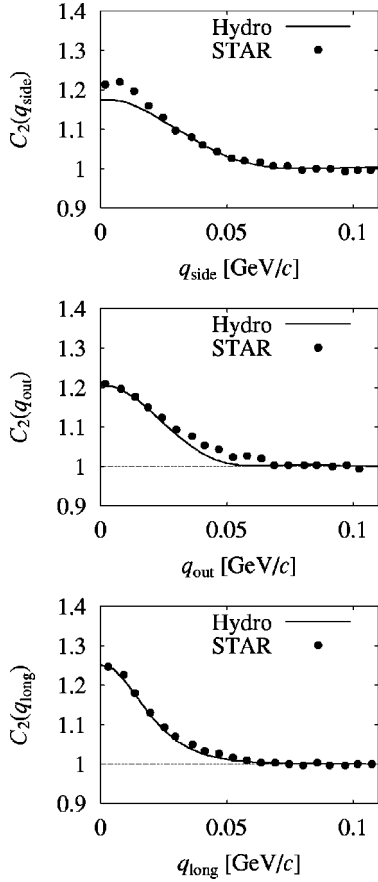|	SPS Pb+Pb	RHIC Au+Au
Net baryon number	305	131
Mean freeze-out temperature	123.2 MeV	125.0 MeV
Mean chemical potential at freeze-out $\langle \mu_B \rangle$	281.6 MeV	76.1 MeV
Mean transverse flow velocity $\langle v_T \rangle$ of the fluid at $|\eta| < 0.1$	0.467c	0.509c
Lifetime of the QGP phase τ_{QGP}	2.67 fm/c	2.92 fm/c
Lifetime of the mixed phase τ_{MIX}	11.12 fm/c	12.61 fm/c
Total lifetime of the fluid τ_{HAD}	17.74 fm/c	18.94 fm/c

FIG. 21. Correlation functions projected onto each component of relative momenta. From top to bottom, sideward, outward, and longitudinal correlation functions are displayed, respectively. Each correlation function is integrated from 0 to 35 MeV with respect to the other two components and corrected by a common λ factor.

Our results show very good agreement with the SPS result, while the RHIC data clearly show different behavior. As concerns the behaviors of R_{out} and R_{out}/R_{side}, an opaque source [37] is a possible explanation if the current formalism of the two-particle correlation is correct. Though the opaque property appears in the hydrodynamical model by virtue of a transverse flow [40], it is still insufficient to reproduce the small R_{out} in the RHIC experiment. More theoretical investigation will be required to solve the problem [20,41].

Figure 21 shows the correlation functions projected onto each component of relative momenta. The transverse momentum of an emitted pair is $0.125 \leqslant K_T \leqslant 0.225$ GeV/c, which corresponds to the lowest momentum bin in Fig. 20. In each figure, calculated correlation functions are corrected by a common factor as $\lambda = 0.6$. The other kind of reduction of the correlation function at $q_i = 0$ ($i =$ side, out, long) is caused by an integration with respect to other components of

the relative momenta. The resultant factor is in proportion to $1/R_i$. Our correlation function seems to be consistent with the experimental data for the outward and the longitudinal directions in spite of the overestimation of the HBT radii. Because the HBT radii correspond to the inverse width of the correlation function, the difference in width between $R = 7$ fm and $R = 6$ fm is only about 5 MeV in relative momentum. The small value of the sideward correlation function at $q_{side} = 0$ indicates that outward and longitudinal HBT radii are larger than the experimental results.

V. CONCLUDING REMARKS

In this paper, we investigated single-particle distributions and two-particle correlation functions in SPS Pb+Pb 17A GeV collisions and RHIC Au+Au 130A GeV collisions based on a hydrodynamical model in which both longitudinal and transverse expansion are taken into account. As far as the single-particle spectra are concerned, the hydrodynamical model describes well both SPS and RHIC data. The initial parameter set in the model for both collisions indicates that initial energy density in the RHIC is only slightly higher than the one in the SPS and a much larger extent of hot matter is produced in the RHIC, if we compare them at the same initial time and by similar initialization [Fig. 3 and Eqs. (11) and (12)]. We have also discussed the space-time evolution of the fluids. Since the initial conditions are not very different, temperature and transverse flow evolution do not shows significant difference between the SPS and the RHIC. Only the equitemperature contour of $T = 158$ MeV shows the qualitative difference between SPS and the RHIC due to the difference in net baryon number density. A steeper pressure gradient in the longitudinal direction at the SPS makes the deviation from the scaling solution larger than at the RHIC. Two-pion correlation functions and the HBT radii are also investigated. Our model shows good agreement with the SPS data. For RHIC data, however, the outward and longitudinal HBT radii of our result are larger than the experimental data even though the dynamical longitudinal expansion and finite size effect are incorporated.

[1] *Quark Matter 2001, Proceedings of the 15th International Conference on Ultra-Relativistic Heavy Ion Collisions*, edited by T. J. Hallman, D.E. Kharzeev, J.T. Mitchell, and T. Ullrich (North-Holland, Amsterdam, 2002); Nucl. Phys. **A698**, 1c

(2002).

[2] J.D. Bjorken, Phys. Rev. D **27**, 140 (1983).

[3] H. von Gersdorff, L. McLerran, M. Kataja, and P.V. Ruuskanen, Phys. Rev. D **34**, 794 (1986); M. Kataja, P.V. Ruus-

kanen, L. McLerran, and H. von Gersdorff, *ibid.* **34**, 2755 (1986).

[4] Y. Akase, M. Mizutani, S. Muroya, and M. Yasuda, Prog. Theor. Phys. **85**, 305 (1991); S. Muroya, H. Nakamura, and M. Namiki, Prog. Theor. Phys. Suppl. **120**, 209 (1995).

[5] J. Alam, S. Raha, and B. Sinha, Phys. Rep. **273**, 243 (1996).

[6] U. Ornik, M. Plümer, B.R. Schlei, D. Strottman, and R.M. Weiner, Phys. Rev. C **54**, 1381 (1996).

[7] C.M. Hung and E.V. Shuryak, Phys. Rev. C **57**, 1891 (1998).

[8] P.F. Kolb, J. Sollfrank, and U. Heinz, Phys. Rev. C **62**, 054909 (2000).

[9] T. Ishii and S. Muroya, Phys. Rev. D **46**, 5156 (1992).

[10] P.F. Kolb, P. Huovinen, U. Heinz, and H. Heiselberg, Phys. Lett. B **500**, 232 (2001).

[11] D. Zschiesche, S. Schramm, H. Stöcker, and W. Greiner, Phys. Rev. C **65**, 064902 (2002).

[12] S.A. Bass and A. Dumitru, Phys. Rev. C **61**, 064909 (2000).

[13] D. Teaney, J. Lauret, and E.V. Shuryak, Phys. Rev. Lett. **86**, 4783 (2001).

[14] D. Teaney, J. Lauret, and E.V. Shuryak, nucl-th/0110037.

[15] T. Hirano, K. Morita, S. Muroya, and C. Nonaka, Phys. Rev. C **65**, 061902(R) (2002).

[16] U.A. Wiedemann and U. Heinz, Phys. Rep. **319**, 145 (1999).

[17] R.M. Weiner, Phys. Rep. **327**, 249 (2000).

[18] S. Soff, S.A. Bass, and A. Dumitru, Phys. Rev. Lett. **86**, 3981 (2001); S. Soff, S.A. Bass, D.H. Hardtke, and S.Y. Panitkin, *ibid.* **88**, 072301 (2002).

[19] U. Heinz and P. Kolb, Nucl. Phys. **A702**, 269 (2002).

[20] T. Humanic, nucl-th/0203004.

[21] C. Nonaka, E. Honda, and S. Muroya, Eur. Phys. J. C **17**, 663 (2000).

[22] F. Cooper and G. Frye, Phys. Rev. D **10**, 186 (1974).

[23] J. Sollfrank, P. Koch, and U. Heinz, Z. Phys. C **52**, 593 (1991).

[24] T. Hirano, Phys. Rev. Lett. **86**, 2754 (2001).

[25] K.J. Eskola, K. Kajantie, and P.V. Ruuskanen, Eur. Phys. J. C **1**, 627 (1998).

[26] T. Hirano, Phys. Rev. C **65**, 011901(R) (2002).

[27] K. Adcox *et al.*, PHENIX Collaboration, Phys. Rev. Lett. **87**, 052301 (2001).

[28] H. Appelshäuser *et al.*, NA49 Collaboration, Phys. Rev. Lett. **82**, 2471 (1999).

[29] A. Wuosmaa *et al.*, PHOBOS Collaboration, Nucl. Phys. **A698**, 88 (2002).

[30] C. Adler *et al.*, STAR Collaboration, Phys. Rev. Lett. **87**, 112303 (2001).

[31] J. Velkovska *et al.*, PHENIX Collaboration, to be published in the Proceedings for International Conference on Physics and Astrophysics of Quark-Gluon Plasma (ICPAQGP-2001).

[32] I.G. Bearden *et al.*, BRAHMS Collaboration, Phys. Rev. Lett. **87**, 112305 (2001).

[33] E.V. Shuryak, Phys. Lett. **44B**, 387 (1973).

[34] Y. Hama and S.S. Padula, Phys. Rev. D **37**, 3237 (1988).

[35] S. Chapman, P. Scotto, and U. Heinz, Phys. Rev. Lett. **74**, 4400 (1995); S. Chapman, J.R. Nix, and U. Heinz, Phys. Rev. C **52**, 2694 (1995).

[36] D.H. Rischke and M. Gyulassy, Nucl. Phys. **A608**, 479 (1996).

[37] H. Heiselberg and A.P. Vischer, Eur. Phys. J. C **1**, 593 (1998).

[38] C. Blume *et al.*, NA49 Collaboration, Nucl. Phys. **A698**, 104c (2002).

[39] C. Adler *et al.*, STAR Collaboration, Phys. Rev. Lett. **87**, 082301 (2001).

[40] K. Morita, S. Muroya, H. Nakamura, and C. Nonaka, Phys. Rev. C **61**, 034904 (2000). In this paper, we used a simpler hydrodynamical model than the present paper; we did not take account of baryon number nor particle productions through the resonances. The EoS is also different.

[41] L. McLerran and S.S. Padula, nucl-th/0205028.